E. Nizery *et al.*, Philosophical Magazine, 95 (2015) 2731-2746

Three dimensional characterization of fatigue relevant intermetallic particles in high-strength aluminium alloys using synchrotron X-ray nanotomography

E. Nizery[a,b,c,*], H. Proudhon[a], J.-Y. Buffière[b], P. Cloetens[d], T. F. Morgeneyer[a], and S. Forest[a]

[a] *MINES ParisTech, PSL - Research University, MAT - Centre des Matériaux, CNRS UMR 7633, BP 87, 91 003 Evry, France*
[b] *Université de Lyon, MATEIS, CNRS UMR 5510, 69 621 Villeurbanne Cedex, France*
[c] *Constellium Technology Center, BP27, 38341 Voreppe Cedex, France*
[d] *European Synchrotron Radiation Facility, BP 220, 38 043 Grenoble Cedex, France*

Abstract

Second-phase particles and small porosities are known to favor fatigue crack initiation in high-strength aluminium alloys 2050-T8 and 7050-T7451. Using high-resolution X-ray tomography (320 nm voxel size), with Paganin reconstruction algorithms, the probability that large clusters of particles contain porosities could be measured for the first time in 3D, as well as precise 3D size distributions. Additional holotomography imaging provided improved spatial resolution (50 nm voxel size), allowing to estimate the probability of finding cracked particles in the as-received material state. The extremely precise 3D shape (including cracks) as well as local chemistry of the particles has been determined. This experiment enabled unprecedented 3D identification of detrimental stress risers relevant for fatigue in as-received aluminium alloys.

Keywords: aluminium alloys, intermetallics, X-ray tomography, 3D characterization, fatigue crack initiation

*Corresponding author
Email address: erembert.nizery@mines-paris.org (E. Nizery)

1. Introduction

Intermetallic particles are known to play a keyrole during the fatigue crack initiation period in structural aluminium alloys (1; 2; 3; 4). Typical dimensions of the particles observed in Rolling Direction - Transverse Direction (RD-TD) plane are in the range $1 - 20\,\mu m$. Their two-dimensional (2D) size distribution has been shown to have a major effect on fatigue life (3; 5; 6). However, fatigue crack initiation is a three-dimensional (3D) mechanism for which dimensions of particles in the third dimension is important (7). Focused Ion Beam (FIB) is a destructive and time-consuming technique, dedicated to small volumes typically $(10\,\mu m)^3$, which is not appropriate for obtaining a statistically 3D representative distribution. Previous studies using X-ray tomography were performed with a voxel size of $0.7\,\mu m$, which already provided good estimate of size distribution (8), although with such a resolution the exact shape cannot be resolved precisely. This prevents the determination of precise stress concentration which may be a key parameter for fatigue crack initiation.

In the last years, several materials science studies utilized X-ray tomography with micrometer like resolution to get an insight on the 3D role of the microstructure on mechanical behaviors. Studies were led *e.g.* on titanium alloys (9), magnesium (10), aluminium alloys (11), and polymers (12). Developments in magnified holotomography at the European Synchrotron Radiation Facility (ESRF) makes it possible to perform 3D imaging of these particles and porosities, with a resolution as low as 50 nm (13), which allows to detect cracked particles (14). Holotomography was already used on a AlMg7.3Si3.5 aluminium alloy by Tolnai et al. (15) to study the effect of solution heat treatment.

High- and nano-resolution tomography is thus expected to provide new information relevant to fatigue crack initiation in aluminium alloys. This paper aims at extracting this information for alloys 2050-T8 and 7050-T7451 using improved voxel sizes of respectively 320 nm and 50 nm. Materials and methods are first introduced, then results obtained respectively with high- and nanoresolution tomography are separately presented and finally discussed.

2. Materials and methods

2.1. Materials

Plates of rolled aluminium alloys 2050-T8 and 7050-T7451 of thickness 60 mm and 65 mm, respectively, were provided by Constellium for this study.

Table 1 gives the material chemical compositions. Both materials contain particles formed during casting process and further deformed during thermo-mechanical heat-treatments. Due to this complex history, the second phase particles end up with a very intricate shape and composition, and are known to influence the fatigue life. A 2D Scanning Electron Microscope (SEM) Energy Dispersive X-ray spectroscopy (EDX) characterization has been conducted on particles of both plates. Among the few tens of particles analyzed in the 2050-T8 plate, only Al–Cu–Fe–Mn were detected. They are divided into Cu-rich and Mn-rich phases, also observed by Ma et al. (16) in a 2099-T8 plate. The plate in 7050-T7451 contains only Al_7Cu_2Fe and Mg_2Si particles, which is consistent with those usually reported in the literature for such Al-Zn alloys (17; 18). Typical dimension for the larger particles in RD-TD plane is around 20 µm equivalent diameter. Cavities of a few microns are also detected. Low stress concentration specimens aligned with the rolling direction from plate in 2050-T8 show improved fatigue lifetime compared to those from plate in 7050-T7451.

	%Cu	%Zn	%Li	%Mg	%Mn	%Ag	%Zr	%Si	%Fe
2050-T8	3.2-3.9	<0.25	0.7-1.3	0.2-0.6	0.2-0.5	0.2-0.7	0.06-0.14	<0.08	<0.1
7050-T74	2.0-2.6	5.7-6.7	-	1.9-2.6	<0.1	-	0.08-0.15	<0.12	<0.15

Table 1: Chemical composition (wt%) of the studied plates.

2.2. Data acquisition

Both high- and nano-resolution imaging of particles and porosities in the two alloys were conducted on the nano-imaging end station of beamline ID22 NI (ESRF, Grenoble). A monochromatic X-rays beam at 29.6 keV was used. Pixel size for nano-resolution holotomography (resp. high-resolution tomography) was 50 nm (resp. 320 nm) (Figure 1). The detector on beamline ID22 is composed of a CCD camera with a 2048 × 2048 pixels area. The total volume analyzed is thus a cylinder of 102.4 µm diameter and 102.4 µm height (resp. 655.4 µm). For holotomography, the procedure to achieve reconstruction of phase contrast requires 4 scans (each one composed of 2000 radiographs). These scans are acquired at four distances between the specimen and CCD detector.

High- and nano-resolution images have been performed on one 2050-T8 Al-alloy and one 7050-T7451 Al-alloy specimen. Both have z-direction

aligned with rolling direction (RD). Cylindrincal 0.6 mm diameter specimens were cut at 1/4 thickness for the tomographic inspection.

Given the typical size, the volume fraction and the spatial repartition of particles, the nano-resolution imaging of a random zone would, in most cases, fail to contain a dense particle-bearing zone. To center the high resolution scans on a particular zone containing particles, the following method apparented to zoom tomography (13) has been used:

- a single high-resolution scan is performed (655 µm containing several hundreds of particles $> 10\,\mu m$),
- a few slices are reconstructed.
- the displacement of the specimen is carefully calculated to align the chosen zone with beam and rotation axis.
- nano-tomography imaging is then carried out.

A quick overview of the experiment is shown in Fig. 1.

2.3. Methods for high-resolution data analysis

2.3.1. From 3D size distribution to 2D equivalent diameter

Reconstructed 32 bit images with voxel size 320 nm are first converted to 8 bit using the following bounds: -436 to 406 for Al2050 and -457 to 457 for Al7050. Voids, particles and matrix are then segmented using gray levels thresholding. For the plate in 2050-T8, all particles are considered to be Al–Cu–Fe–Mn (the only particles detected by EDX analysis in section 2.1). For the plate in 7050-T7451, particles darker than the matrix (inversed colors) contain elements heavier than the matrix, and correspond therefore to Al_7Cu_2Fe. On the contrary, the brighter particles correspond to Mg_2Si. Inhouse ImageJ plugins are then used to label and compute the 3D size distributions. The equivalent ellipsoid of particles larger than 10 microns and all voids larger than 2 microns are also determined (19).

One of the goals of this work is to evaluate possible errors in terms of particle and void size distributions from surface inspections.2D and 3D particle equivalent diameters distributions have not the same physical units (number of particles per mm^2 and per mm^3 respectively). Some tools have been used in the literature to overcome this limitation (20; 21; 22), and stereology (23) provided a framework to transform 2D distributions into 3D ones based on

the knowledge of 3D shapes. In this paper, we propose an alternative method to transform 3D data into 2D distributions.

For a given material, two different methods are used and compared to provide a 2D distribution from 3D data.

1. The first method (which is equivalent to observing a polished surface, called here 'real') consist in analyzing size distribution in many RD-TD planes of the 3D labeled images.
2. The second method (called here 'ideal') assumes that we cut many slices through a volume where each particle has been replaced by its equivalent ellipsoid with parameters a, b and c. The particles are assumed to be aligned with the rolling direction RD, as observed for both alloys.

For both methods, 2000 slices have been analyzed which correspond to the full 3D stack and to a total surface of 690 mm^2. For each slice, 2D equivalent diameters of particles present in this slice (intersected) are computed. Note that with the first method, a particle with a non convex shape may lead to several islands on the slice cut through the volume and thus to several equivalent diameter.

2.3.2. Particles and void clusters

In this study, a cluster is defined as a set of particles and porosities composed by elements closer than a distance D (the surface distance is considered). For each tomographic volume, the computation of particles and void surface distances in 3D requires 6 hours using 12 cores and 100 Gb. Then, the clusters are constructed as follows:

1. Let a set contain one particle or one porosity (not contained in any previously constructed cluster),
2. every particle or porosity which distance (surface-to-surface) to an element of the set is below D = 0.96 microns (3 voxels) is added to the set,
3. the previous step is repeated until no element can be further added. The final set constitutes a new cluster.

2.4. Methods for 50 nm voxel size magnified holotomography data analysis

2.4.1. 3D particle shape

As before, thresholding of particles and porosities is carried out on holotomography 3D images. The surfaces used for precise 3D morphology visualization, are obtained with Avizo software. Fractured particles are detected

with magnified holotomography. Fractures have platelet shapes, and can be therefore clearly distinguished from spherical porosities.

2.4.2. Local particle density

In tomography, when phase-contrast reconstructions are used, gray levels are proportional to electron density (24) – number of electrons per unit volume, so that the gray level of a phase can be correlated with the elements that it contains.

In this study we will assume that electron density is proportional to weight density. In both alloys, void and matrix densities are well known (zero for voids and 2.71 to 2.83 for the Al-matrix, depending on the alloy). Using the letters d and g for respectively densities and gray levels, and remembering that gray levels linearly depend on the electron density (*i.e.* linearly depend on the weight density in a first approximation), the formula providing the density of an intermetallic particle is then easily obtained with proportionality rules:

$$d_{particle} = \frac{g_{particle} - g_{porosity}}{g_{matrix} - g_{porosity}} \times d_{matrix} \quad (1)$$

3. High-resolution tomography: results

In this part, results produced by high-resolution tomography are presented: statistical data about size distributions of (i) particles and (ii) porosities, and (iii) proximity of particles and porosities.

Contrary to Al–Cu–Fe–Mn particles presented in (8) (classical tomography with voxel size 0.7 µm), the 3D reconstruction method employed here do not produce dark or bright artefact rings around particles and porosities: errors concerning the nature of particles and porosities are therefore excluded.

3.1. 2D and 3D particles and porosities distributions

Statistical 3D particle distributions obtained using 320 nm voxel size tomography are presented in Fig. 2a. In the plates studied here, Mg_2Si particles are much smaller than either Al_7Cu_2Fe or Al–Cu–Fe–Mn, which have size distributions of the same order of magnitude. The plate in 2050-T8 contains particles Al–Cu–Fe–Mn slightly larger than particles Al_7Cu_2Fe of 7050-T7451. Integrating these distributions gives the total number of particles > 10 µm in both alloys ($\sim$2300/mm^3 for 2050 plate and $\sim$3400/mm^3 for

7050 plate), and the volume fraction (∼0.65% for Al–Cu–Fe–Mn, ∼0.78% for Al_7Cu_2Fe and ∼0.15% for Mg_2Si).

The comparison between the 'real' and 'ideal' two-dimensional distributions on plane RD-ND (Fig. 2.b) highlights that in the real case (what we actually observe on 2D surfaces) the number of small particles is overestimated and the number of large particles is simultaneously underestimated, compared to the case where particles are assumed not to have compex shapes (ellipsoids).

On reconstructed 3D slices (Fig. 1) porosities are visible in both alloys. The maximum size of porosities deduced from the size distribution is about 10 µm equivalent diameter for both plates (Fig. 3), and the volume fractions lie near 0.015%. 2D measurements failed at obtaining a similar distribution on polished surfaces due to their small size (statistically few on a given slice) and the fact that porosities may be filled during polishing. A Scanning Electron Microscope (SEM) image of one particle situated near porosities is obtained in the 2050-T8 plate (Fig. 4): one of the porosities is filled.

3.2. Clustering of particles and porosities

Results presented here were calculated using a critical distance between particles and porosities of $D = 3$ voxels (0.96 µm). In order to obtain a contact criterion between particles and porosities, D should be as low as possible. During the thresholding of particles and porosities, an error of one or two voxels might appear: a minimum acceptable value is therefore arbitrarily fixed at 3 voxels. Since results are almost identical when increasing D to 6 voxels and 9 voxels, the critical value is kept at 3 voxels.

Using the algorithm described in § 2.3, three main results concerning particles and small porosities clusters are obtained (Fig. 5):

1. First, for clusters containing both particles and porosities, the larger the cluster (*i.e.* the particles), the larger the porosities inside (Figure 5b).
2. Second, the larger the cluster, the higher the probability that it contains a porosity. When considering porosities larger than 4 µm (mean position of the peak in the 3D porosities size distribution in 2050-T8 and 7050-T7451 plates) the probability is larger than 50% for clusters larger than 20 µm, and reaches almost 100% for clusters larger than 35 µm. The probability is slightly higher in 2050 plate compared to 7050 plate (Figure 5a).

3. Third, the larger the porosity, the higher the probability that it lies in a cluster. When considering particles larger than 15 µm (three times the critical size for fatigue initiation reported in the literature (7; 25)) the probability is larger than 50% for porosities larger than 6 µm, and is almost 100% for those larger than 10 µm. The results are very similar in both alloys (Figure 5c).

In this analysis, it is shown that large particles are most of the time in contact with a porosity. This point will be discussed later, since the larger particles are more likely to initiate fatigue cracks in the studied plates as well as in similar aluminium alloys (25; 26).

4. 50 nm voxel size magnified holotomography: results

The previous section detailed information that can be obtained with high-resolution tomography. We now focus on holotomography with voxel size 50 nm.

4.1. Particle cracking

Using phase contrast in holotomography, it is possible to visually distinguish cracked and non-cracked particles (Fig. 6), as already observed by Requena et al. (14) on a SiC particle contained in the 2124/SiC/25p metal matrix composite. The studied volume is small ($8.4 \cdot 10^{-4}$ mm^3), so that only a small number of particles is analyzed here. In the 2050-T8 plate, two Al–Cu–Fe–Mn particles are cracked: both of them are in contact with a porosity, and the crack in the particle is connected with the porosity (visualization on Fig. 7, left). A last porosity is observed, which separates a particle in two independent parts: it could be considered itself as a crack. For the plate in 7050-T7451, three cracked Mg_2Si particles – which are known to fracture easily (27) – are identified, and no Al_7Cu_2Fe. For two of the cracked Mg_2Si, no porosity is observed in their vicinity. For the third one, two porosities are in contact with the particle, however, they are not connected with the cracks in it. A last porosity is situated near a non-cracked Al_7Cu_2Fe particle (Fig. 7, right).

Errorbars representing effective 80% confidence interval (taking into account the number of particles studied) are calculated (28). From these observations, it is possible to plot the fraction of cracked particles prior to loading *vs* the 3D equivalent diameter. Two conclusions can be drawn (Fig. 8): (i)

the cracking probability during the process is different depending on the type of particle (Mg_2Si, Al_7Cu_2Fe, Al–Cu–Fe–Mn), (ii) large particles are more likely to be cracked.

4.2. Particle density measured with holotomography

On Fig. 9, gray levels corresponding to the peaks maximums are associated with particles. As in section 2.3.1, the peak of voxels with a gray level lower than the gray level of the matrix is associated with Cu-rich particles. In the 7050-T7451 plate, the peak with a higher gray level is associated with Mg_2Si particles. Applying the formula from equation 1 to the light gray particles in the 7050 plate provides a mass-density of 2.09. The error due to the assumption that electron density is proportional to weight density is expected below $\pm 7\%$ (see appendix). The real density measured for Mg_2Si is 1.99 (29). For dark particles in the 7050 plate, a density of 4.25 has been found, which should be compared to the value 4.30 measured by Bown and Brown (30) for Al_7Cu_2Fe particles. Therefore, measurements displayed in Table 2 can be considered with a precision better than 10%. Applying the formula to Cu-bearing particles in the 2050-T8 plate, which properties are unknown, shows that their density is similar to that obtained for Al_7Cu_2Fe.

Phase	Matrix 2050	Matrix 7050	Cu-rich Al–Cu–Fe–Mn	Al_7Cu_2Fe	Mg_2Si	porosity 2050	porosity 7050
$d_{measured}$	2.71	2.83	–	4.30 ± 0.08	1.99	0	0
$d_{calculated}$	–	–	–	4.10 ($a = 0.64$, $b = 1.48$)	2.0 ($a = 0.635$)	0	0
gray level (32-bits)	-3	-3	-444	-417	212	752	823
$d_{holotomo}$	–	–	4.29 ± 0.43	4.25 ± 0.43	2.09 ± 0.21	–	–

Table 2: Comparison of density measured in the literature ($d_{measured}$) (29; 30), calculated thanks to lattice parameters ($d_{calculated}$), and measured using holotomography gray-levels ($d_{holotomo}$).

5. Discussion

In this study, the smallest diameters considered for particles and porosities are around 3 µm. Since for a voxel of 0.32 µm the resolution lies empirically near 0.64 µm, high-resolution tomography appears to be adapted for

the present statistical analysis: while lower resolution would not have been sufficient, higher resolution would imply a too small analyzed volume (*i.e.* less representativity). On the other hand, holotomography allows to analyze very precisely a small number of particles and porosities.

We discuss here the data obtained with high-resolution and 50 nm voxel size magnified holotomography, regarding fatigue properties.

At the macroscopic level, 2D particle distributions (sometimes only extreme value distributions) are classically used to compare alloys and are sometimes used in mathematical models to predict fatigue lifetime (31). Though, the measured 2D distributions have been now experimentally shown to underestimate the number/size of large particles (Fig. 2), which are the most relevant for the study of fatigue crack initiation. This is attributed to the fact that large particles with 3D complex shapes might be considered as many small ones with 2D observations. Thus, when 2D distributions of particles from different plates are compared, it should be verified or assumed that the bias introduced by 2D observations is the same. The bias induced by the complex shape of particles is significant in both alloys in RD-ND plane, therefore, retrieving 3D distributions from 2D ones should be done carefully. In this study, 3D distributions of particles are directly measured for both alloys, which provides reliable data.

At the microscopic level, fatigue crack initiation on flat surfaces in commercial alloys may happen to be related with local stress concentration risers as cracked particles, or large porosities (31).

In the literature, the role of cracked particles on fatigue crack initiation in rolled aluminium alloys is shown to be important (6; 32), including for the studied plates (33). In these studies, some particles are cracked in as-received plates, and other may crack during mechanical loading. This paper shows that particles of both plates may be cracked in the as-received volume (Fig. 6), and the probability of cracking increases with their 3D size and depends on their type (Mg_2Si, Al_7Cu_2Fe, Al–Cu–Fe–Mn) (Fig. 8). This 3D analysis completes those of the literature which are only on 2D polished surfaces (6; 33), and both results (dependence on size and type) are consistent with them. It should be noticed that cracked particles detected with the nanotomography technique could not be observed with a SEM in this study: nanotomography provided a 3D image of the inside of the specimen, and thus an extremely high precision polishing would have been required for SEM sample preparation. No direct comparison of cracked particles images by SEM and nanotomography is therefore available yet, either here or in the

literature.

Since the type of particles has an influence on the propensity of cracking, their properties are very important while difficult to access. One of them, the density, has been obtained with holotomography in the present study. It has been shown that despite their different cracking probability Al–Cu–Fe–Mn and Al_7Cu_2Fe particles have similar densities.

Small porosities as described in this study were not underlined as effective fatigue crack initiation sites in the literature. Two explanation are proposed: (i) such porosities are less detrimental than cracked particles, and (ii) they may be located a few microns under the surface investigated.

The proximity of particles and small porosities has not been investigated in the past for such aluminium alloys. In this paper, we show that the larger particles, which are believed to initiate fatigue cracks, are very likely to stay in contact with a small porosity. Even if no significant effect on fatigue initiation has been attributed to small porosities in the literature, the lack of 3D experiments may hide their role, which might be coupled with that of particles. The fact that cracks in all three Al–Cu–Fe–Mn particles observed with holotomograhy start at porosities could indicate that, for Al–Cu–Fe–Mn particles in the 2050-T8 plate, the presence of porosities could be correlated with particle cracking.

6. Summary

High-resolution tomography provided particle and porosity size distributions and showed that porosities are statistically located near large particles. The error made on 2D distributions obtained on surfaces has been quantified. A voxel size of 320 nm is identified as an appropriate resolution for 3D statistical studies of the distribution/cluster of particles and porosities, which are involved in fatigue crack mechanisms in 2050-T8 and 7050-T7451 plates.

With *nano-resolution* the proximity of cracked particles and small porosities could be visualized precisely. This provided real 3D data about microscopic stress concentration risers that may lead to fatigue crack initiation: mesh can be extracted and further used in Finite Element analysis. Nano-resolution tomography also enables the measurement of microscopic particles densities.

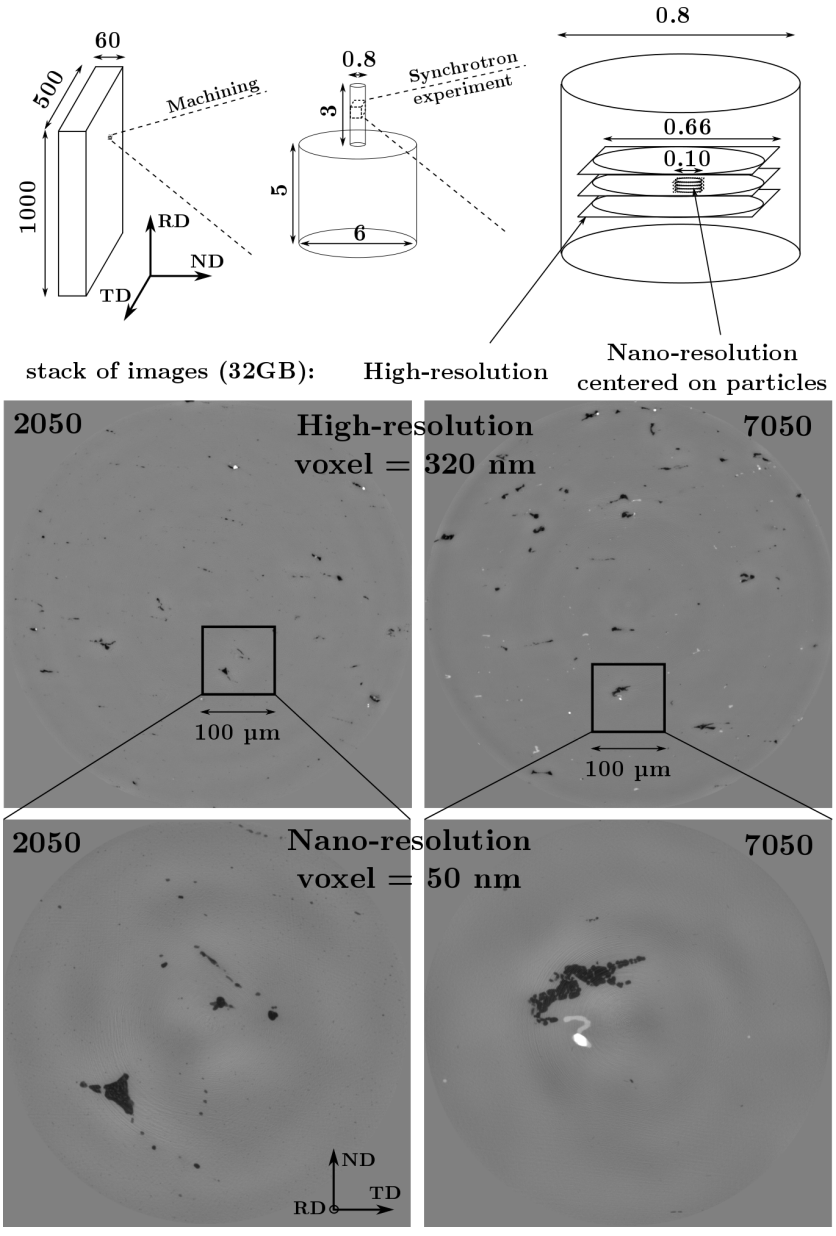

Figure 1: (a) Quick overview from process leading to nano-resolution images from an industrial plate (dimensions in mm), (b) 320 nm-resolution and 50 nm-resolution images from particles contained in 2050-T8 and 7050-T7451 plates (colors are inversed compared to SEM images and classical tomography: particles are in dark).

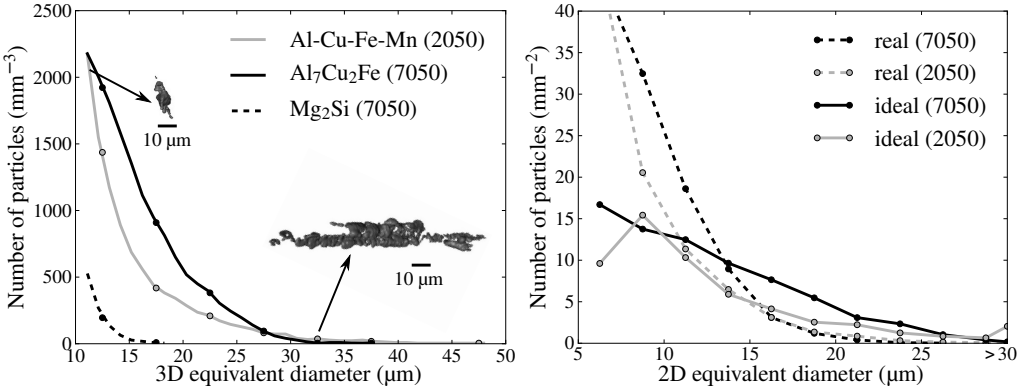

Figure 2: (a) 3D size distribution of Al–Cu–Fe–Mn particles (2050-T8), Al_7Cu_2Fe and Mg_2Si particles (7050-T7451) (plot bin width = 5 µm), (b) comparison between 3D and 2D distributions on RD-ND plane: 'ideal' means that particules are considered as ellipsoids, whereas 'real' refers to image analysis on real slices (plot bin width = 2.5 µm).

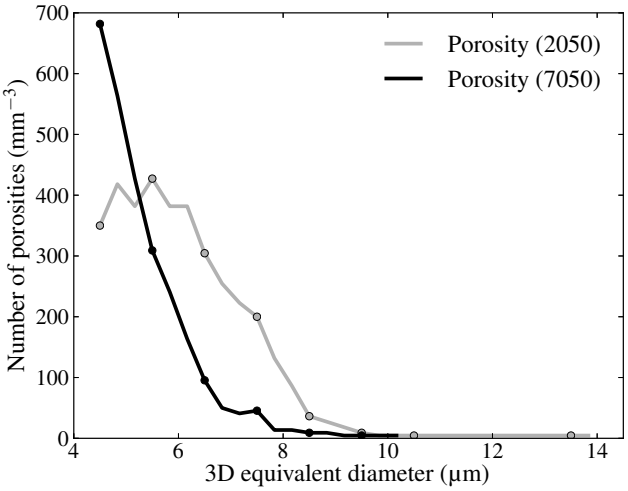

Figure 3: 3D porosities size distribution contained in 2050-T8 and 7050-T7451 plates (plot bin width = 1 µm).

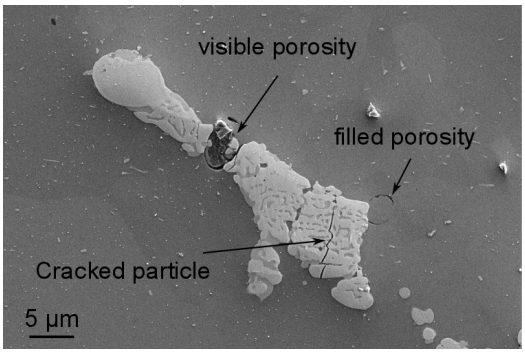

Figure 4: (2050-T8 plate) SEM-SE micrograph of an Al–Cu–Fe–Mn particle. A porosity is visible in the center of the particle, but due to polishing some are almost not distinguishable (dark circle reveals a filled porosity).

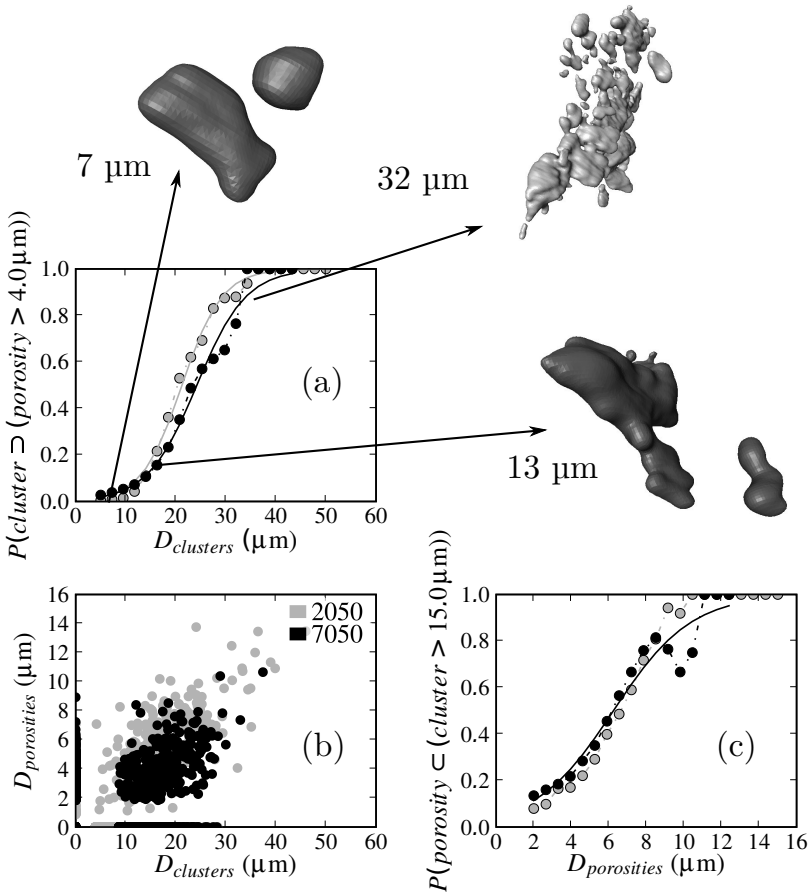

Figure 5: (a) Probability for a large particle to contain a porosity, and Al–Cu–Fe–Mn particles visualization from the 2050-T8 plate, (b) Size of porosities relative to the cluster size it is contained in, (c) Probability for a porosity to lie near a large particle.

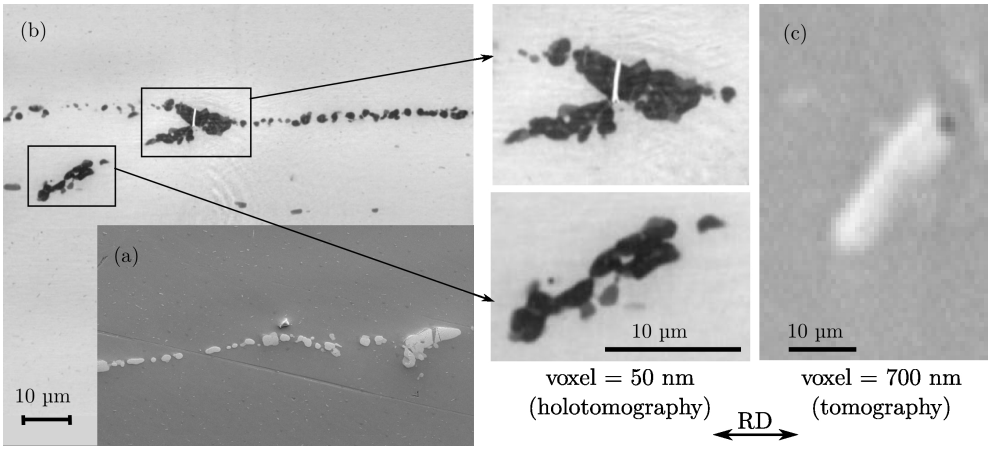

Figure 6: Comparison of images in RD-TD plane (2050-T8 plate) between (a) SEM-Secondary Electrons imaging, (b) a slice obtained with the holotomography technique (inversed colors: particles are in dark), and (c) a slice obtained with high-resolution tomogragphy.

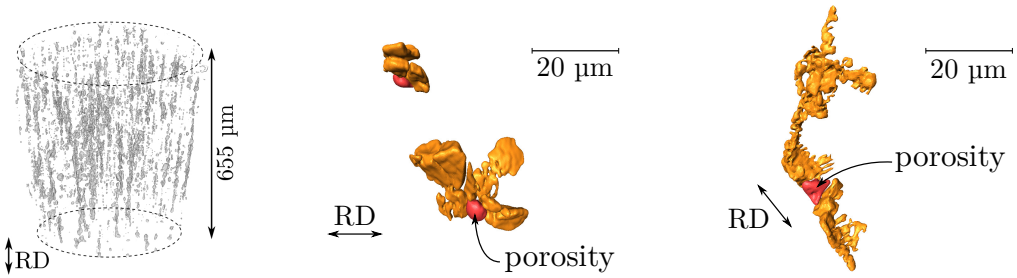

(a) 2050-T8 (b) 2050-T8 (c) 7050-T74

Figure 7: 3D surface visualization of particles (gray/orange) and porosities (red) with high-resolution (subfigure a), and nano-resolution (subfigure b and c). On subfigure b, a crack in the particle begins at the porosity.

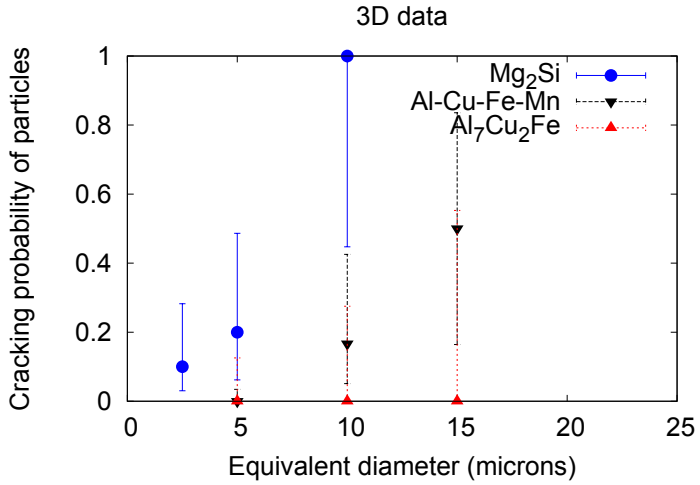

Figure 8: Cracking probability of particles in as-reveived 2050-T8 and 7050-T7451 plates with respect to their nature and 3D equivalent diameter (80% Wilson's confidence interval (28)).

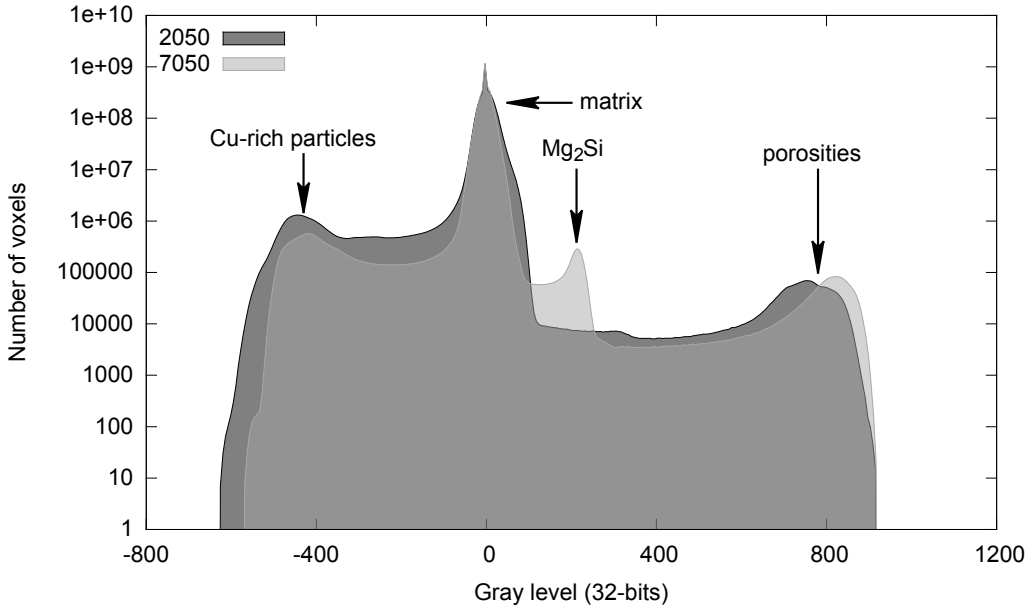

Figure 9: Gray level distribution in reconstructed volumes of 2050-T8 and 7050-T7451 specimens. Peaks positions are quantitatively related to particles densities.

7. Acknowledgment

We would like to thank Constellium Technology Center for providing the material used in this study. We acknowledge the European Synchrotron Radiation Facility for providing beamtime (experiment 1647).

8. References

[1] J. C. Grosskreutz, G. G. Shaw, Critical mechanisms in the development of fatigue cracks in 2024-t4 aluminium, in: Fracture 1969, Pergamon Press, Brighton, 1969, pp. 620–629.

[2] S. Pearson, Initiation of fatigue cracks in commercial aluminium alloys and the subsequent propagation of very short cracks, Eng. Fract. Mech. 7 (2) (1975) 235–247.

[3] S. Suresh, Fatigue of materials, Cambridge University Press, Cambridge; New York, 1998.

[4] L. Farcy, C. Carre, M. Clavel, Y. Barbaux, D. Aliaga, Factors of crack initiation and microcrack propagation in aluminum lithium 2091 and in aluminum 2024, J. Phys. Colloq. 48 (C3) (1987) 3–3.

[5] T. Sanders, J. T. Staley, Review of fatigue and fracture research on high-strength aluminium alloys, in: Fatigue and microstructure, ASM, 1978, pp. 467–516.

[6] J. Payne, G. Welsh, R. J. Christ, J. Nardiello, J. M. Papazian, Observations of fatigue crack initiation in 7075-t651, Int. J. Fatigue 32 (2) (2010) 247–255.

[7] W. Wen, A. H. Ngan, Y. Zhang, B. Xu, T. Zhai, A study of the effects of particle 3-dimensional geometry and micro-texture on fatigue crack initiation behaviors in an al-cu alloy using focused ion beam and electron backscatter diffraction, Mater. Sci. Eng. A 564 (2013) 97–101.

[8] J. Delacroix, Etude des mecanismes de fissuration en fatigue et/ou fretting d'alliages al-cu-li, Ph.D. thesis, INSA Lyon, France (2011).

[9] S. Birosca, J. Y. Buffiere, F. A. Garcia-Pastor, M. Karadge, L. Babout, M. Preuss, Three-dimensional characterization of fatigue cracks in ti-6246 using x-ray tomography and electron backscatter diffraction, Acta Mater. 57 (19) (2009) 5834–5847.

[10] A. King, W. Ludwig, M. Herbig, J.-Y. Buffiere, A. A. Khan, N. Stevens, T. J. Marrow, Three-dimensional in situ observations of short fatigue crack growth in magnesium, Acta Mater. 59 (17) (2011) 6761–6771.

[11] H. Proudhon, A. Moffat, I. Sinclair, J.-Y. Buffiere, Three-dimensional characterisation and modelling of small fatigue corner cracks in high strength al-alloys, C. R. Phys. 13 (3) (2012) 316–327.

[12] L. Laiarinandrasana, T. F. Morgeneyer, H. Proudhon, F. N'guyen, E. Maire, Effect of multiaxial stress state on morphology and spatial distribution of voids in deformed semicrystalline polymer assessed by x-ray tomography, Macromolecules 45 (11) (2012) 4658–4668.

[13] R. Mokso, P. Cloetens, E. Maire, W. Ludwig, J.-Y. Buffiere, Nanoscale zoom tomography with hard x-rays using kirkpatrik-baez optics, Appl. Phys. Lett. 90 (14) (2007) 144104.

[14] G. Requena, P. Cloetens, W. Altendorfer, C. Poletti, D. Tolnai, F. Warchomicka, H. P. Degischer, Sub-micrometer synchrotron tomography of multiphase metals using Kirkpatrick-Baez optics, Scripta Mater. 61 (7) (2009) 760–763.

[15] D. Tolnai, G. Requena, P. Cloetens, J. Lendvai, H. P. Degischer, Sub-micrometre holotomographic characterisation of the effects of solution heat treatment on an AlMg7. 3Si3. 5 alloy, Mater. Sci. Eng. A 550 (2012) 214–221.

[16] Y. Ma, X. Zhou, G. E. Thompson, T. Hashimoto, P. Thomson, M. Fowles, Distribution of intermetallics in an AA 2099-t8 aluminium alloy extrusion, Mater. Chem. Phys. 126 (1) (2011) 46–53.

[17] W. L. Morris, The effect of intermetallics composition and microstructure on fatigue crack initiation in al 2219-t851, Metall. Mater. Trans. A 9A (1978) 1345–1348.

[18] Y. Xue, H. El Kadiri, M. F. Horstemeyer, J. Jordon, H. Weiland, Micromechanisms of multistage fatigue crack growth in a high-strength aluminum alloy, Acta Mater. 55 (2007) 1975–1984.

[19] E. Maire, N. Gimenez, V. Sauvant-Moynot, H. Sautereau, X-ray tomography and three-dimensional image analysis of epoxy-glass syntactic foams, Philos. T. Roy. Soc. A 364 (1838) (2006) 69–88.

[20] J.-H. Han, D.-Y. Kim, Analysis of the proportionality constant correlating the mean intercept length to the average grain size, Acta Metall. Mater. 43 (8) (1995) 3185–3188.

[21] R. L. Fullman, Measurement of particle sizes in opaque bodies, Trans. AIME 197 (1953) 447–452.

[22] N. Limodin, L. Salvo, M. Suéry, F. Delannay, Assessment by microtomography of 2D image analysis methods for the measurement of average grain coordination and size in an aggregate, Scripta Mater. 60 (5) (2009) 325–328.

[23] J. Russ, R. Dehoff, Practical stereology, Plenum Press, New York, 1999.

[24] P. Cloetens, W. Ludwig, J. Baruchel, D. Van Dyck, J. Van Landuyt, J. Guigay, M. Schlenker, Holotomography: Quantitative phase tomography with micrometer resolution using hard synchrotron radiation x rays, Appl. Phys. Lett. 75 (1999) 2912.

[25] P. J. Laz, B. M. Hillberry, Fatigue life prediction from inclusion initiated cracks, Int. J. Fatigue 20 (4) (1998) 263–270.

[26] C. Y. Kung, M. E. Fine, Fatigue crack initiation and microcrack growth in 2024-t4 and 2124-t4 aluminum alloys, Metall. Mater. Trans. A 10 (5) (1979) 603–610.

[27] Y. Shen, T. F. Morgeneyer, J. Garnier, L. Allais, L. Helfen, J. Crépin, Three-dimensional quantitative in situ study of crack initiation and propagation in AA6061 aluminum alloy sheets via synchrotron laminography and finite-element simulations, Acta Mater. 61 (7) (2013) 2571–2582.

[28] A. Agresti, B. A. Coull, Approximate is better than 'exact' for interval estimation of binomial proportions, Am. Stat. 52 (2) (1998) 119–126.

[29] E. E. Schmid, K. von Oldenburg, G. Frommeyer, Microstructure and properties of as-cast intermetallic Mg2Si-Al alloys, Z. Metallkd. 81 (11) (1990) 809–815.

[30] M. G. Bown, P. J. Brown, The structure of FeCu2Al7 and t (CoCuAl), Acta Crystallogr. 9 (11) (1956) 911–914.

[31] Y. Murakami, Metal fatigue : effects of small defects and nonmetallic inclusions, 1st Edition, Elsevier, 2002.

[32] J. E. Bozek, J. D. Hochhalter, M. G. Veilleux, M. Liu, G. Heber, S. D. Sintay, A. D. Rollett, D. J. Littlewood, A. M. Maniatty, H. Weiland, A geometric approach to modeling microstructurally small fatigue crack formation: I. probabilistic simulation of constituent particle cracking in AA 7075-t651, Model. Simul. Mater. Sc. 16 (6) (2008) 065007.

[33] E. Nizery, J. Y. Buffiere, H. Proudhon, A. Daniélou, S. Forest, Influence of particles on short fatigue crack initiation in 2050-t8 and 7050-t74, Mater. Sci. Forum 794-796 (2014) 296–301.

List of Figures

Appendix A. Proportionality between number of electrons and weight of atoms

The chemical elements present in both alloys and in the particles studied in this paper are mainly: Al, Cu, Mg, Zn, Li, Mn, Ag, Zr, Fe, Si. As shown in Figure A.10, the number of nucleons can be estimated from the number of electrons by the mean of a linear approximation. Values used for chemical elements are those reported in periodic tables. The error induced by such an approximation is below ±7%.

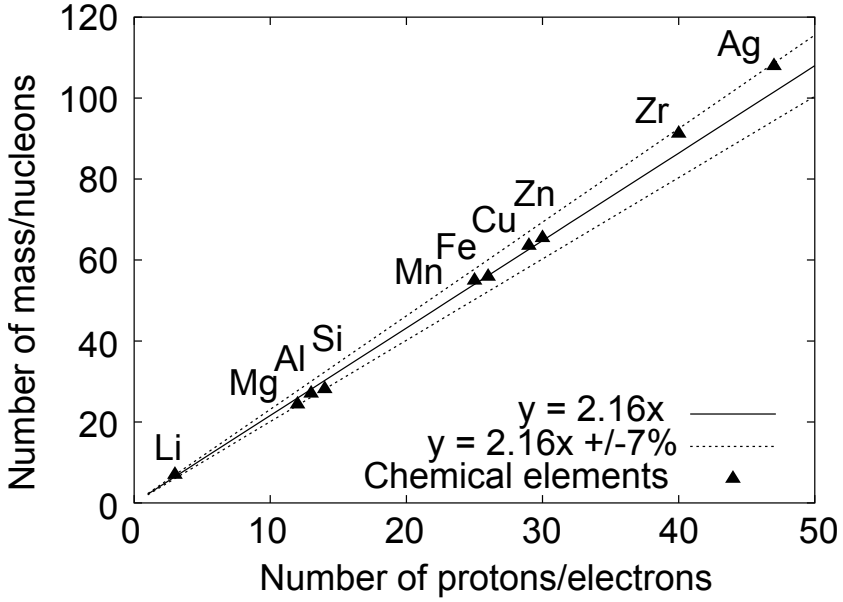

Figure A.10: The number of mass of an atom is correlated with its number of electrons. For the elements contained in the studied alloys, the linear approximation $y = 2.16x$ provides an error of less than ±7%.